



Article

A Bayesian Hydrometeor Classification Algorithm for C-Band Polarimetric Radar

Ji Yang ^{1,2}, Kun Zhao ^{1,2,*}, Guifu Zhang ³ , Gang Chen ^{1,2}, Hao Huang ^{1,2}  and Haonan Chen ⁴

¹ Key Laboratory for Mesoscale Severe Weather/MOE and School of Atmospheric Science, Nanjing University, Nanjing 210003, China

² State Key Laboratory of Severe Weather and Joint Center for Atmospheric Radar Research of China Meteorological Administration and Nanjing University, Chinese Academy of Meteorological Sciences, Beijing 100081, China

³ School of Meteorology and Advanced Radar Research Center, University of Oklahoma, Norman, OK 73072, USA

⁴ Cooperative Institute for Research in the Atmosphere, Colorado State University, Fort Collins, CO 80523, USA

* Correspondence: zhaokun@nju.edu.cn; Tel.: +86-025-8968-2539

Received: 10 July 2019; Accepted: 7 August 2019; Published: 12 August 2019



Abstract: A hydrometeor classification algorithm is developed by applying Bayes' theorem to C-band polarimetric weather radar measurements. The Bayesian hydrometeor classification algorithm (BHCA) includes eight hydrometeor types: hail, rain, graupel, dry snow, wet snow, crystal, biological scatterers (BS) and ground clutter (GC). The conditional likelihood probability distribution functions (PDFs) for each hydrometeor type are constructed with training data from radar observations. The prior PDFs include not only temperature information but also background information about occurrence frequency of hydrometeor types at each altitude, which is incorporated by a hydrometeor classification algorithm for the first time. The BHCA is evaluated by comparing with the Marzano-Bayesian hydrometeor classification algorithm (MBHC) and NCAR fuzzy logic classifier (NFLC). Results show that wet snow is largely missed in MBHC, while crystals are not adequately identified by NFLC. This may be due to the inappropriate conditional likelihood PDFs or membership functions. The prior PDFs in the MBHC may cause unexpected hail due to unreasonable variation above 0 °C. In addition, the prior PDFs of graupel and dry snow in the MBHC appear below −52 °C, which is not realistic. The BHCA proposed in this study overcomes these shortcomings in the prior PDFs and produces an overall reasonable classification product over the Yangtze-Huaihe River Basin (YHRB), Eastern China.

Keywords: hydrometeor classification; polarimetric radar; Bayes' theorem; prior PDFs; conditional likelihood

1. Introduction

Dual-polarization weather radar can offer various variables including horizontal reflectivity (Z_H), differential reflectivity (Z_{DR}), the cross-correlation coefficient (ρ_{hv}), and specific differential phase (K_{DP}), providing indicative information about hydrometeor size, shape, orientation, concentration and phase [1]. Based on this information, hydrometeor classification (HC) can be achieved [2,3], which leads to various important applications. For example, it can be used to resolve cloud microphysical processes [4,5], perform severe weather surveillance and nowcast involving different precipitation phases [6,7], and remove nonweather echoes (e.g., biological scatterers and ground clutter) for data quality control [8]. Furthermore, according to the identified hydrometeor types, appropriate rain rate relations can be derived to improve quantitative precipitation estimation [9].

For S-, C- and X-band polarimetric radars, the most popular HC algorithms are based on the fuzzy logic method [3,10–17], which used the temperature information and polarimetric radar variables as input. The most important component in the fuzzy logic method is the membership functions which show high overlap between several particle types [10–12,18,19]. The membership functions employed alternative functions including trapezoidal [11], beta [12], Gaussian [20], and half-Gaussian [21] functions, which may introduce errors since the shapes of functions are pre-assumed. In addition, radar measurement errors and random fluctuations are unavoidable and should not be ignored [22]. These issues may result in a noisy output classification, leading to severe weather warning false alarm (e.g., hail) for forecaster, and/or misleading information in the microphysical processes for research and other applications with HC products. Improvement and optimization in the classification scheme is very important for such applications, especially for timely decision-making during rapid evolution convective events.

In addition to the characteristics of hydrometeors observed by radar and associated temperature information, occurrence frequencies of different hydrometeor types can be used as background information that can be incorporated in the HC algorithms. A Bayesian approach [23,24] is an appropriate choice for HC since it can naturally take into account the information mentioned previously. As such, this study aims to develop a robust HC algorithm based on Bayes' theorem.

Marzano et al. [24] developed a Bayesian HC algorithm (MBHC), where the conditional likelihood probability distribution function (CLPDF) is constructed with joint probability distribution functions (PDF) of Z_H - Z_{DR} - K_{DP} or Z_H - Z_{DR} derived from T-Matrix scattering simulations. Although their work proves that the Bayesian approach is a practical method for HC, there are still several limitations in their Bayesian HC framework: (1) useful information indicated by ρ_{hv} , the standard deviations of horizontal reflectivity ($SD(Z_H)$) and differential propagation phase shift ($SD(\Phi_{DP})$) were not taken into account in [24]. These three variables show substantial capability in identifying ground clutter and biological scatterers [11,25]. (2) Inevitable radar measurement biases and random errors, which may introduce misclassification, are not included in the T-Matrix simulation. In addition, the T-Matrix simulations depend on observed particle size distributions from disdrometers, which may introduce errors because of different spatial representativeness between the radar and disdrometer. (3) The prior PDF in [24] may not be sufficient. In their method, if several hydrometeor types are allowed to appear in a given temperature range, the occurrence frequencies were set equal to each other. That is, the prior PDF in [24] is not a continuous function along with temperature or in the vertical dimension, which may result in unrealistic classification. The Bayesian hydrometeor classification algorithm (BHCA) developed in this paper is expected to improve these issues to produce a robust HCA product for practical applications [23,24,26].

This paper is organized as follows: instruments and data processing are introduced in Section 2. The theoretical background of Bayesian approach and the construction of conditional PDFs and prior PDFs are described in Section 3. The classification results and cross-comparison with previous algorithms are presented in Section 4, and the conclusions are given in Section 5.

2. Instruments and Data

Radar data collected by Nanjing University C-band polarimetric radar (NJU C-POL) during the Observation, Prediction and Analysis of Severe Convection of China (OPACC) field campaign from 1 June to 31 July in 2014 are employed in this study [27,28]. The OPACC was conducted over the Yangtze-Huaihe River Basin (YHRB) in East China. Closely related to the Asian summer monsoon, major rainfall over YHRB occurs from mid-June to mid-July [29]. The datasets include a squall line with trailing stratiform precipitation, mesoscale convective systems, isolated convective cells, and typhoon rainbands, which encompass the eight hydrometeor types considered in this study and main rainfall types over the YHRB. NJU C-POL is a research mobile radar. The scanning strategy is configured with a volume coverage pattern (VCP) mode including plan position indicator (PPI) scans at 14 elevation angles (0.5° , 1.5° , 2.4° , 3.4° , 4.3° , 5.3° , 6.2° , 7.5° , 8.7° , 10.0° , 12.0° , 14.0° , 16.7° and 19.5°)

completed within seven minutes followed by a vertically-pointing Z_{DR} calibration scan. Range-height indicator (RHI) scans are performed manually if there is intense convection. The azimuthal and radial resolutions are 1.2° and 75 m, respectively. The maximum range is 144 km. For RHI scans, the maximum elevation is 30° . More details about the system characteristics of NJU C-POL are listed in [28]. A sphere calibration experiment was conducted to ensure low system biases of Z_H and Z_{DR} . The dataset for validation is processed by the MBHC and NCAR fuzzy logic classifier (NFLC) which use K_{DP} as input. The K_{DP} is estimated from differential propagation phase shift by piecewise linear regression using a least square fit following Wang and Chandrasekar [30]. Attenuation is corrected with the linear relation with KDP [31].

3. The Bayesian Hydrometeor Classification Method

In the BHCA, five radar variables— Z_H , $Z_H - Z_{DR}$, ρ_{hv} , $SD(Z_H)$, and $SD(\Phi_{DP})$ —are chosen as inputs. Z_H and Z_{DR} are used as joint probability since they are not independent in rain. $SD(Z_H)$ and $SD(\Phi_{DP})$ are calculated along the radial direction over five gates centered on the current gate. Eight hydrometeor classes are defined in the BHCA, namely, hail (HA), rain (RN), graupel (GR), dry snow (DS), wet snow (WS), crystals (CR), biological scatterers (BS) and ground clutter (GC). The training dataset for the CLPDFs and prior PDFs are based on the data collected during 13:04–15:06 LST (LST = UTC + 8) on June 1, 09:05–11:08 LST on July 15, 06:05–06:59 and 15:24–16:27 LST on 24 July, 2014, including both RHI and PPI data.

3.1. Bayesian Classification Concept

Bayes' theorem was applied in the Bayesian classifier, with the assumption that five variables were mutually independent for eight classes. The formula was given as follows:

$$P(C_i|V_1, \dots, V_5) = \frac{P(C_i)P(V_1, \dots, V_5|C_i)}{P(V_1, \dots, V_5)}, \quad (1)$$

where C_i represents a hydrometeor class; V_1, \dots, V_5 denote variables Z_H , $Z_H - Z_{DR}$, ρ_{hv} , $SD(Z_H)$ and $SD(\Phi_{DP})$, respectively; $P(C_i)$ is the prior PDF; and $P(V_m|C_i)$ is the CLPDF. Each V_m is assumed to be conditionally independent on any other V_n ($n \neq m$). $P(V_1, V_2, V_3, V_4, V_5)$ is assumed to be a constant. Thus, Equation (1) is transformed into

$$P(C_i|V_1, \dots, V_5) \propto P(C_i) \prod_{i=1}^5 SF_i \prod_{i=1}^5 P(V_m|C_i), \quad (2)$$

where SF represents scaling factor for normalizing the CLPDFs. According to the above equation, the conditional probability $P(C_i|V_1, \dots, V_5)$ of each hydrometeor class at each range volume can be calculated. Essentially, the class with the largest conditional posterior probability $P(C_i|V_1, \dots, V_5)$ will be assigned to the range volume by the classifier.

3.2. The Conditional Likelihood PDFs of Radar Variables

The conditional PDFs and the prior PDFs are crucial components in the Bayesian classifier. One of the advantages of the simple Bayesian classifier is that a relatively small amount of training data is required for the construction of the PDFs. The training and evaluation datasets are strictly separated from each other. Homogeneous areas and "true" hydrometeor types are chosen to construct PDFs by human experts through subjectively checking every polarimetric radar variables. Then, all the PDFs for each variable need to be modeled before applying them to the BHCA. The PDFs show different

shapes, and the best fitting function is chosen for negative skewness (Equation (3)), positive skewness (Equation (4)), and Gaussian shape (Equation (5)):

$$P(V) = aV^b \exp\left(\frac{-c(V^2 - \langle V \rangle)^d}{2\sigma^2}\right), \tag{3}$$

$$P(V) = aV^b \exp\left(\frac{-c(\ln V - \langle V \rangle)^d}{2\sigma^2}\right), \tag{4}$$

$$P(V) = a \exp(-b(V - c)^2), \tag{5}$$

where V stands for input variables; a, b, c and d are the fitting parameters of PDFs given in Table 1, and the modeling functions are showed in Figure 1; and $\langle V \rangle$ and σ^2 denote the mean and variance listed in Table 2. A nonlinear least squares curve fitting method is used to derive these parameters.

Table 1. Fitted function parameters of the likelihood conditional probability for four variables horizontal reflectivity (Z_H), the cross-correlation coefficient (ρ_{hv}), standard deviations of horizontal reflectivity ($SD(Z_H)$) and differential propagation phase shift ($SD(\Phi_{DP})$), and eight hydrometeor classes: hail (HA), rain (RN), graupel (GR), dry snow (DS), wet snow (WS), crystals (CR), biological scatterers (BS) and ground clutter (GC). a, b, c and d stand for parameters in Equations (3)–(5).

Variables	Classes	a	b	c	d	Equation Type
Z_H	HA	2.82×10^{-13}	7.9284	17.327	5.1301	4
	RN	0.0221	1.1047	127.29	1.2649	3
	GR	2578.2	-0.303	17.135	3.9478	4
	CR	0.1546	0.6202	2.9539	1.8152	3
	WS	0.2814	0.3391	10.649	1.6386	3
	DS	0.0660	0.8216	2.51×10^{-6}	4.0119	3
	BS	4427.0	-0.780	0.9446	1.3140	4
	GC	0.6599	0.0033	2.4841	3.6438	4
ρ_{hv}	HA	22.925	1.5322	146.26	4.1906	4
	RN	1	1666.7	1	-	5
	GR	1997.4	24.519	63.508	345.21	4
	CR	1	2272.7	1	-	5
	WS	2.57×10^{-5}	3.5618	0.0009	2.9922	3
	DS	1.3832	-55.32	0.5360	-	5
	BS	150.40	0.4279	0.7031	1.9887	3
	GC	3.5356	0.3638	1.1735	2.3235	3
$SD(Z_H)$	HA	20.909	1.5322	146.26	4.1906	4
	RN	8.9198	-0.8192	0.9361	1.8218	4
	GR	0.8711	-0.6537	1.0669	2.0824	4
	CR	7.4321	-0.7811	0.9452	1.9085	4
	WS	7.4063	-0.7553	0.9222	1.8085	4
	DS	7.4273	-0.7605	0.9196	1.8863	4
	BS	4373.0	-0.0008	0.0014	0.0026	3
	GC	24.942	0.0790	7.6961	-	5
$SD(\Phi_{DP})$	HA	21.816	-0.6041	0.9501	1.5407	4
	RN	3.7498	-1.0723	1.1236	1.8026	4
	GR	75.554	-0.7516	1.0656	1.8232	4
	CR	2.3996	-0.6038	1.2830	1.5799	4
	WS	2.8006	-0.7799	0.8447	1.8268	4
	DS	3.5388	-0.9901	1.1997	1.7305	4
	BS	17587	-1.4781	1.5339	1.9489	4
	GC	3.3987	0.0014	65.92	-	5

Finally, the bivariate Gaussian function is used to fit joint PDFs of Z_H-Z_{DR} :

$$P(x, y) = a \times \exp\left(\left(\frac{-1}{2 \times (1 - \rho^2)}\right)\left(\frac{(V_1 - \langle V_1 \rangle)^2}{\sigma_1^2} - \frac{2\rho(V_1 - \langle V_1 \rangle)(V_2 - \langle V_2 \rangle)}{\sigma_1\sigma_2} + \frac{(V_2 - \langle V_2 \rangle)^2}{\sigma_2^2}\right)\right), \quad (6)$$

where V_1 and V_2 represent Z_H and Z_{DR} , respectively; $\langle V_i \rangle$ and σ_i stand for the mean and variance presented in Table 3. The PDF fitting parameter ρ is the correlation coefficient between Z_H and Z_{DR} . Note that Z_{DR} has large fluctuations for GC. Therefore, this study uses the PDF of Z_H instead of the joint probability of Z_H-Z_{DR} for GC. The identification for GC is not affected by this change because it mainly depends on $SD(Z_H)$ (Figure 1g) and $SD(\Phi_{DP})$ (Figure 1i). Figure 1g and j show the big difference between GC and the other types. These two variables were also used by fuzzy logic methods for identification of GC [8,11,32–34]. The y-scale (Z_{DR}) in Figure 1d has a break and repeats to prevent overlap.

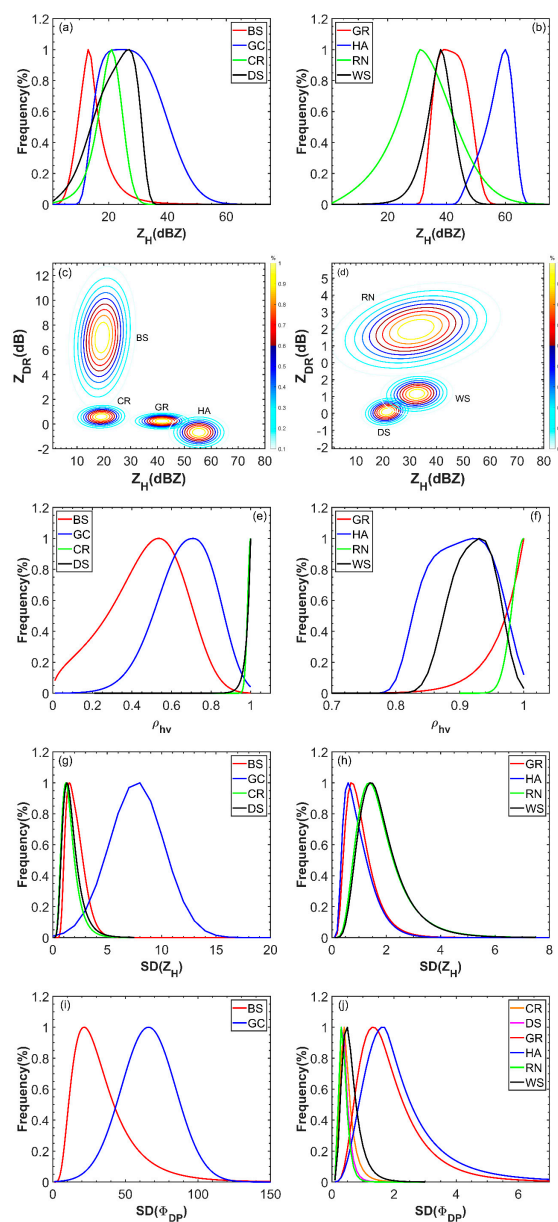


Figure 1. Conditional probability distribution functions (PDFs) fitted with Equations (3)–(6) for polarimetric radar variables: (a,b) Z_H ; (c,d) Z_H-Z_{DR} ; (e,f) ρ_{hv} ; (g,h) $SD(Z_H)$; and (i,j) $SD(\Phi_{DP})$.

Table 2. Mean $\langle V \rangle$, and variance σ^2 of four variables Z_H , ρ_{hv} , $SD(Z_H)$ and $SD(\Phi_{DP})$ and eight classes in Equations (3) and (4). The en-dash indicates that the fitting function is Equation (5) without mean and variance. Values given are the square (for Equation (3)) and the natural logarithm (for Equation (4)) of Z_H [dBZ], Φ_{DP} [degrees], and ρ_{hv} .

Mean and Variance	Classes	Z_H	ρ_{hv}	$SD(Z_H)$	$SD(\Phi_{DP})$
$\langle V \rangle$	HA	3.9700	-0.1118	-0.1665	0.5488
	RN	927.90	-	2.7593	1.2869
	GR	3.7197	-0.0472	-0.1257	0.2706
	CR	421.24	-	0.1993	0.2646
	WS	2079.1	8432.63	2.7739	1.6845
	DS	514.10	-	2.7037	1.3181
	BS	2.6037	0.2571	0.6383	3.5420
	GC	0.1808	0.4905	-	-
σ^2	HA	0.0010	0.0033	0.3662	0.2446
	RN	594.02	-	0.2058	0.1649
	GR	0.0141	0.0026	0.4443	0.2860
	CR	174.94	-	1.0108	1.0273
	WS	648.07	640.08	0.1857	0.1868
	DS	274.76	-	0.2023	0.1980
	BS	0.1285	0.1692	0.1900	0.4959
	GC	0.6668	0.1805	-	-

Table 3. Mean value $\langle V_1 \rangle$ ($\langle V_2 \rangle$) and standard deviation σ_1 (σ_2) for variable Z_H (Z_{DR}) and correlation coefficient ρ in Equation (6).

Classes	$\langle V_1 \rangle$ (dBZ)	σ_1	$\langle V_2 \rangle$ (dB)	σ_2	ρ
HA	55.3953	5.2010	-0.6632	0.6894	0
RN	32.3002	10.0542	2.0739	0.8770	0.1443
GR	41.6840	3.9131	0.2397	0.2555	0
CR	19.0370	3.4456	0.5944	0.3610	0.0303
WS	32.7988	4.5676	1.2486	0.4495	0.0308
DS	21.5010	3.1002	0.2014	0.3119	0.0751
BS	19.3775	4.0815	6.9877	1.8733	0.0847

3.3. The Prior PDFs of Hydrometeor Types

The prior PDFs are usually constructed as a function of temperature [24] because the hydrometeors only exist within certain temperature ranges. In addition to the temperature, occurrence frequency of hydrometeor types at each altitude is also included in the prior PDFs. Considering the weather and non-weather echoes, the prior PDFs of hydrometeor types are designed to be functions of altitude as a compromise for simplification, where the altitude is computed based on the elevation and range gate detected by radar. The prior PDFs of GC and BS are functions of altitude relative to mean sea level, while the others are relative to freezing level.

In this study, for the independence between the training and testing datasets, the C-band hydrometeor identification algorithm (RCHIA) developed by [12] is used to determine the training data along with the subjective selection in order to confirm the HC's reliability. The RCHIA is well tuned and shows a reasonable classification in Eastern China [5]. The fitted PDFs are presented in Table 4 and Figure 2, with the fitting functions based on Equations (3)–(5), and a combination of them for bimodal PDFs.

The BS, GC, WS and DS (Table 4a) show a single peak. CR (RN) almost monotonically increases (decreases) with altitude (Table 4b). The prior PDFs of GR and HA are bimodal (Table 4b). The primary peaks are due to the high altitude, where the stratiform precipitation cannot reach. Therefore, only strong convection could be detected with fewer total points at the high levels than at the low levels.

The secondary peak is due to the most suitable region where GR (HA) develops, causing the largest absolute quantity in the vertical dimension.

Table 4. (a) Fitted function of the prior PDFs for hydrometeor types GC, BS, WS and DS. Altitude for GC and BS is relative to the mean sea level, altitude for WS and DS is relative to the freezing level. (b) Fitted function of the prior PDFs for hydrometeor types: HA, RN, GR and CR. “Altitude” indicates altitude above mean sea level of freezing level.

	Altitude (km)	GC	BS	Altitude (km)	WS	Altitude (km)	DS
a	0.5	7.63×10^{-2}	1.02×10^{-4}	-3	1.43×10^{-6}	-2	0.0
	1	0.140	0.003	-2.5	1.11×10^{-4}	-1	0.010
	1.5	0.196	0.026	-2	0.003	0	0.353
	2	0.210	0.106	-1.5	0.042	1	0.451
	2.5	0.172	1.68×10^{-1}	-1	0.201	2	0.452
	3	0.108	1.06×10^{-1}	-0.5	0.385	3	0.450
	3.5	0.052	2.63×10^{-2}	0	0.293	4	0.448
	4	0.019	2.60×10^{-3}	0.5	8.75×10^{-2}	5	0.445
	4.5	0.005	1.02×10^{-4}	1	1.04×10^{-2}	6	0.432
	5	1.18×10^{-3}	1.58×10^{-6}	1.5	4.90×10^{-4}	7	0.368
	5.5	1.95×10^{-4}	9.69×10^{-9}	2	9.14×10^{-6}	8	0.212
	6	2.47×10^{-5}	2.36×10^{-11}	2.5	6.75×10^{-8}	9	4.87×10^{-2}
	6.5	0	0	3	0	10	1.95×10^{-3}
	7	0	0	3.5	0	11	4.11×10^{-6}

	Altitude (km)	HA	Altitude (km)	RN	Altitude (km)	GR	Altitude (km)	CR
b	-5	0.006	-4.5	0.465	-3	0.002	0	0
	-4	0.011	-4	0.467	-2	0.011	1	6.91×10^{-5}
	-3	0.018	-3.5	0.467	-1	0.045	2	0.002
	-2	0.026	-3	0.462	0	0.139	3	0.010
	-1	0.036	-2.5	0.448	1	0.144	4	0.025
	0	0.047	-2	0.420	2	0.091	5	0.047
	1	0.060	-1.5	0.375	3	0.058	6	0.075
	2	0.077	-1	0.312	4	0.038	7	0.107
	3	0.090	-0.5	0.235	5	0.027	8	0.141
	4	0.062	0	0.156	6	0.058	9	0.175
	5	0.085	0.5	0.089	7	0.169	10	0.208
	6	0.118	1	0.041	8	0.294	11	0.238
	7	0.154	1.5	0.015	9	0.125	12	0.265
	8	0.036	2	0.004	10	0.052	13	0.289
	9	0.023	2.5	0.001	11	0.022	14	0.309
	10	0.006	3	1.12×10^{-4}	12	0.009	15	0.326

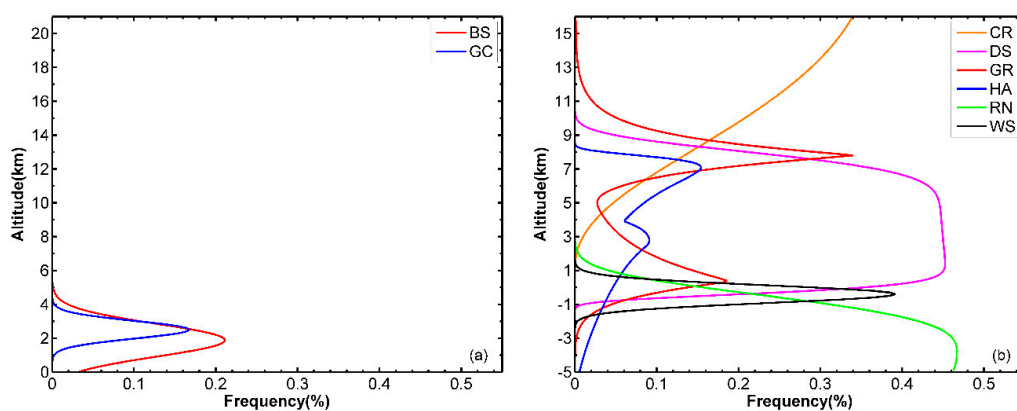


Figure 2. Prior PDFs. Altitude in (a) is relative to the mean sea level, whereas altitude in (b) is relative to the freezing level.

4. Analyses and Results

4.1. Validation Concept

Validation is difficult for all HC methods because in-situ measurements of hydrometeors are difficult to obtain. Therefore, alternative approaches are typically adopted for validation [12,15,21,24,35–38]. For example, observations on the ground were used to verify HCs in winter [35–37]. Automated Surface Observation System and voluntary observations of precipitation types provided by the public can be used as “truth”. If HA falls on the ground in summer, results of HC at low levels can be verified as well. However, for most cases in the YHRB, there is only RN on the ground, with other solid hydrometeor types at higher altitudes. Liu and Chandrasekar [13] and [17] compared results of a HC against in-situ observations collected by High-Volume Particle Spectrometer image probe installed under a T-28 aircraft. This approach is very expensive, and only data on the aircraft trajectory can be verified, but it is the most objective way for validation. A testing dataset was constructed based on simulation [24] or subjective identification [21] for quantitative evaluation of a HC method. According to the uniqueness of certain HC types, other methods can be developed for validation as well. One example was from Snyder and Ryzhkov [15], who developed a fuzzy logic method for detecting tornadic debris signature (TDS) and compared it with tornado tracks for qualitative validation. Comparisons between different HC methods [20] were also performed to evaluate a new HC approach. It is probably not a real evaluation, because HC products from other HC method are not the “truth”, but this is an effective way to see how well the new HC method performs compared to other well-established approaches. Subjective validation was conducted as well, where the microphysics derived from a HC algorithm were compared with human knowledge or conceptual models [3,8,11,12].

Due to the lack of in-situ microphysical measurements in this study, comparisons between the BHCA and MBHC [24] as well as conceptual models seem to be a realistic way for evaluation. There are 10 hydrometeor types in the MBHC but only eight types in the BHCA. It is necessary to combine several hydrometeor types in the MBHC for comparison. In particular, large drops, light rain, medium rain and heavy rain are combined to RN; hail and rain/hail mixture are merged to HA. The other types in MBHC are the same with those in the BHCA. However, it should be noted that the combined types are not exactly the same as the types in the BHCA. In addition, the NFLC is a well-established fuzzy logic method which has been widely used. Comparison with the NFLC [16] (C-band version available at https://ral.ucar.edu/projects/titan/docs/radial_formats/pid_thresholds.cband.shv.txt) is also conducted to evaluate the performance of BHCA. Note that the NFLC is developed with the dataset under a North American climate; it may not perform well over YHRB. In addition, it should be mentioned that any method in this study is not considered as the reference or benchmark. The results from HC methods are mainly discussed with relevant polarimetric radar signatures and microphysical processes. Otherwise, comparison with the NFLC could evaluate the identification of GC and BS which are not included in MBHC. Similarly, drizzle, light rain, moderate rain and heavy rain are combined into RN; hail and rain hail mixture are merged into HA; GR/small HA and GR/RN are combined into GR; ice crystals and irregular ice crystals are combined into CR; supercooled liquid droplets and second trip are combined into other types which are not included in the BHCA.

4.2. Squall Line

On 30 July, 2014, a few isolated thunderstorms initiated north of Hefei, Anhui Province in the afternoon. A few hours later, these isolated cells merged, and more convection occurred, eventually became a squall line with trailing stratiform region in the evening. Figure 3a–d shows the NJU C-POL observations at 4.3° elevation angle during this squall line. The squall line is characterized by the trailing stratiform region with an obvious embedded bright band (BB). Figure 3e–g shows the classification results of the BHCA, MBHC and NFLC, respectively. Generally, they show good agreement.

Below the freezing level (blue circle in Figure 3), BB can be obviously seen from Figure 3a–d as indicated by increased Z_H and Z_{DR} and decreased ρ_{hv} in the stratiform precipitation near the freezing

level. Most of these signatures are identified by the BHCA and the NFLC, while the MBHC only detects several pixels of WS and much GR and RN in the BB. The evaluation of [24] showed that the classification accuracy (hits) of WS is also low (55%), indicating the CLPDF of WS in the MBHC may not be robust. The poor performance of WS identification may be related to large uncertainty in modelling the melting hydrometeor [39]. The NFLC also identifies several areas of GR (black rectangles in Figure 3g), which seem not realistic. Above the freezing level, the BHCA, MBHC and NFLC identify similar areas of DS, which agrees well with the polarimetric radar signatures with moderate Z_H (20–30 dBZ), small Z_{DR} (< 1 dB), and high ρ_{hv} (> 0.97). The DS and RN identified by the MBHC (Figure 3f) are strictly separated by the freezing level, indicating that these two hydrometeor types strongly depend on temperature. The DS and RN identified by the BHCA (Figure 3e) seem more realistic near the freezing level than those identified by the MBHC (Figure 3f).

The polarimetric radar signatures within convection show high Z_H (40–50 dBZ), low Z_{DR} (< 1 dB), and high ρ_{hv} (> 0.94), indicating GR or small HA. These signatures are reasonably identified as GR by the BHCA, MBHC and NFLC. In the convection core, there are some pixels that show higher Z_H (~55 dBZ), low Z_{DR} (< 1 dB), high K_{DP} (> 4°) (not shown) and low ρ_{hv} (< 0.9), which are all indicators of HA. The classification results from the three methods are roughly consistent (Figure 3e–g) in this area.

Figure 4 shows the RHI scan for the squall line along the black dash line in Figure 3. The output classifications identified by the three methods show some differences. Within the strong convection at range ~90 km, polarimetric radar variables show increased Z_{DR} (> 0.75 dB) and large Z_H (> 45 dBZ) extended above 6 km, indicating supercooled liquid water is lifted by strong updrafts [40], resulting in riming of GR and the growth of small HA. Therefore, a large area of GR is expected, but discontinuous GR, and HA mixed with DS in the area are identified by the MBHC. The DS type in the MBHC is only related to the Z_H and temperature. Furthermore, the CLPDF may not include appropriate measurement biases and random fluctuations, which may introduce a noisy output. On the contrary, the BHCA and NFLC provide much more reasonable output classifications of GR in this area. In addition, a small area of WS is identified by the NFLC within the weak convection. The microphysical process of the weak convection by polarimetric radar signature is riming rather than melting, and similar to the strong one at ~90 km range, indicating that the WS within the weak convection identified by the NFLC may not be reasonable.

Below the freezing level, more HA is identified by the MBHC relative to the BHCA. It is hard to tell which is closer to the truth without in-situ measurements. However, we want to note that HA is a rare weather phenomenon over the YHRB. As a result, the CLPDF and prior PDF for HA may not be sufficient. Improvements should be made by incorporating more HA observations in the future. Another obviously different output classification is the WS. As the DS particles fall below the melting layer, they begin to melt at different rates, resulting in water coated on their exterior or sucked inward to the vertices, causing increases in Z_H , Z_{DR} and a decrease in ρ_{hv} . The polarimetric radar signatures show a clear BB within the stratiform region, most of which are identified by the BHCA and NFLC. The MBHC detects much GR and several pixels of WS in this area. Although rimed aggregates left over from collapsing deep convection or produced by Kelvin-Helmholtz instability, which are difficult to distinguish using polarimetric radar, could exist within stratiform regions [41], the main BB signature is missed by the MBHC. Within the BB at range <20 km, the radar signatures present strong Z_H (> 50 dBZ) and low ρ_{hv} (< 0.85), which are nearly beyond the membership function in the fuzzy logic method or CLPDF in the Bayesian approach. This is likely due to snow melting and strong rimming of aggregates. Both the BHCA and NFLC identify GR in most of this area.

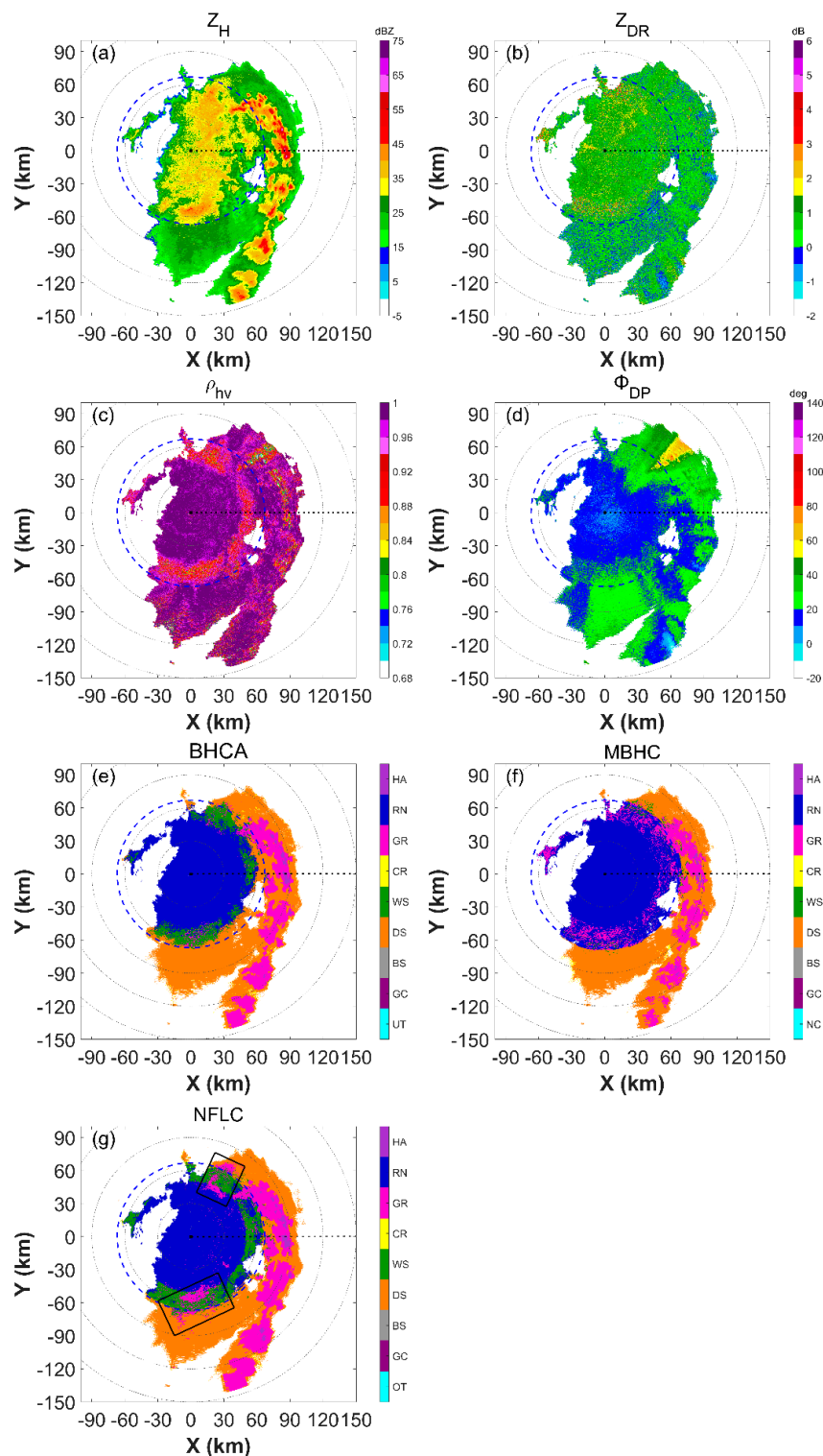


Figure 3. Plan position indicator (PPI) of (a) Z_H , (b) Z_{DR} , (c) ρ_{hv} , (d) Φ_{DP} , and corresponding hydrometeor classification results by (e) the Bayesian hydrometeor classification algorithm (BHCA), (f) Marzano-Bayesian hydrometeor classification algorithm (MBHC) and (g) NCAR fuzzy logic classifier (NFLC) at 4.3° elevation angle at 23:04 LST on 30 July 2014. The blue dash circle represents freezing level determined from sounding data, and the black dash line shows the azimuth of range-height indicator (RHI) scan in Figure 4. The black rectangles highlight the different output classification. Each range ring represents 30 km distance of interval away from radar site.

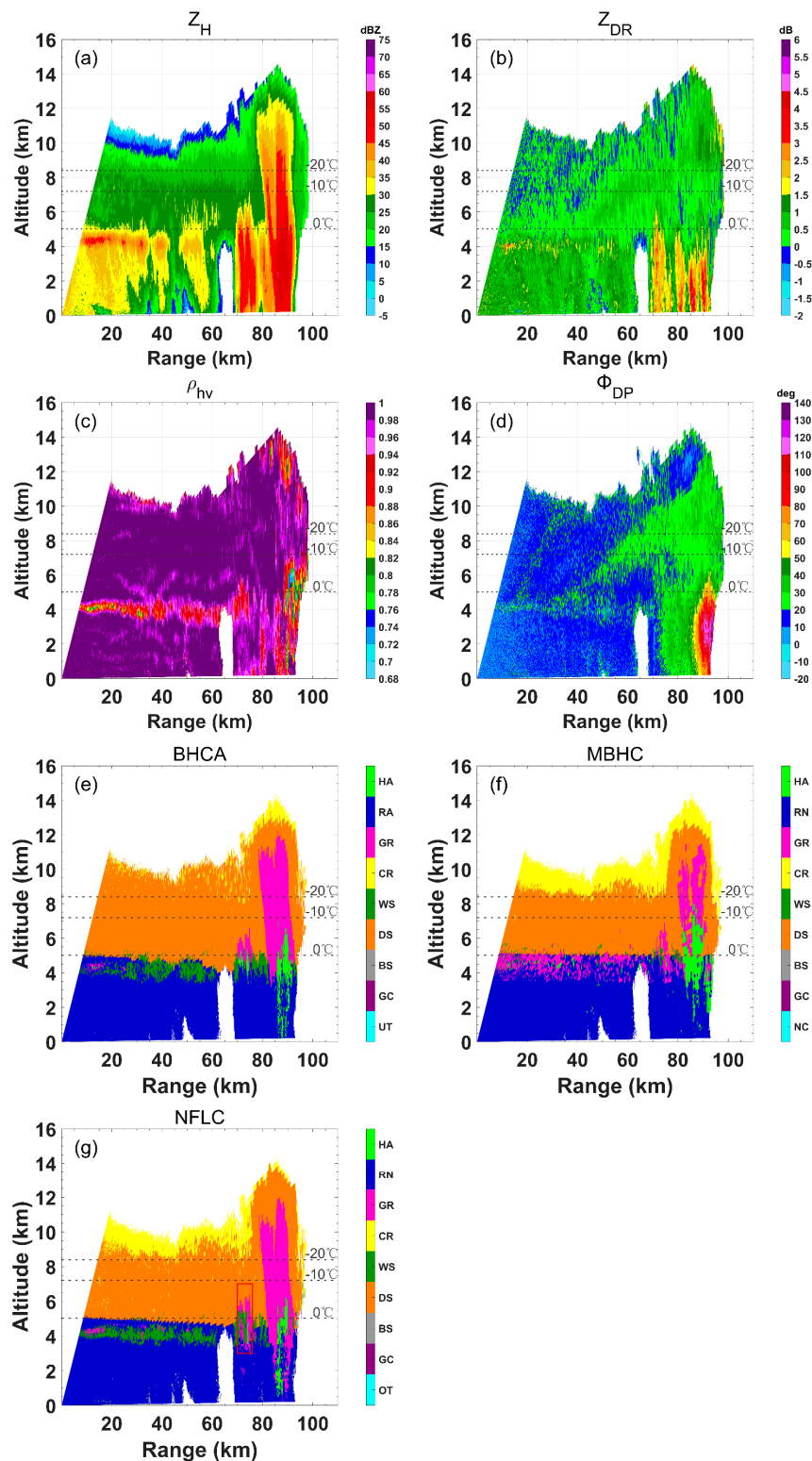


Figure 4. Range-height indicator (RHI) of (a) Z_H , (b) Z_{DR} , (c) ρ_{hv} , (d) Φ_{DP} , and corresponding hydrometeor classification results by the (e) Bayesian hydrometeor classification algorithm (BHCA), (f) Marzano-Bayesian hydrometeor classification algorithm (MBHC) and (g) NCAR fuzzy logic classifier (NFLC) at 89.93° azimuth along black dash line in Figure 3, at 23:11 LST on 30 July 2014. The black dashed lines represent the temperature level of 0 °C, −10 °C and −20 °C from bottom to top, respectively. The red rectangle highlights the different classification results.

Above the freezing level, the dominant polarimetric radar signatures present moderate Z_H (20–30 dBZ), small Z_{DR} (< 1 dB), and high ρ_{hv} (> 0.98), which indicate DS. In this area, the BHCA identifies predominant DS and a small area of CR on the edge of the convection and a few pixels of CR within the stratiform region. The MBHC detects dominant DS and large area of CR on the edge of the convective and stratiform region. The NFLC also identifies a large area of CR within the stratiform region, but nearly no CR identified within the convection. This is because the same membership function for temperature is used for DS and CR in the NFLC, resulting in some vagueness in the boundary between them. While the prior PDFs of CR in the BHCA and MBHC show obvious differences from that of DS, it is difficult to quantify which is closer to the truth without in-situ measurements. Nevertheless, this difference reflects the different prior PDF and CLPDF or membership functions used in the three methods.

4.3. Isolated Deep Convection

At 20:19 local solar time on 11 July, 2014, isolated strong convection occurred at 128.6° azimuth angle to the radar site. Available RHI scan (Figure 5) data are used to evaluate the BHCA. Figure 4a–d show the convection extending above 18 km AGL. A 40 dBZ echo reaches 14 km AGL, indicating large number of solid hydrometeors lifted by a strong updraft. The BHCA and NFLC identify large areas of GR (Figure 5e,g) extending above 16 km, which are consistent with the polarimetric signature of GR with high Z_H (40–50 dBZ), low Z_{DR} (< 1 dB), and high ρ_{hv} (> 0.94). The GR (Figure 5f) detected by the MBHC reaches about 13 km AGL (altitude of -52 °C in this case) with a short horizontal linear edge. Because GR is excluded by the prior PDF in the MBHC below -52 °C, the prior PDF for GR is not suitable for this case. In addition, almost no CR is identified by the NFLC in Figure 5 (red rectangle), which seems unrealistic.

There is a noticeable phenomenon that much more HA is identified by the MBHC (Figure 5f) at altitude near 3 km than the altitude between 4 and 5 km. The sounding data shows that temperature near 3 km is higher than 10 °C, which is not a suitable environment for riming or deposition for HA growing, but is in favor of melting for HA. The large area of HA may be contributed by the larger prior PDF between 3 and 10 °C than that between 0 and 3 °C. On the edge of the strong convection, there are echoes with strong Z_H (> 50 dBZ), large Z_{DR} (> 3dB), low ρ_{hv} (< 0.94). These signatures suggest HA/RN mixture, most of which are not identified by the BHCA below 2 km AGL. The MBHC and NFLC identify a small part of the HA/RN mixture. As mentioned previously, the training dataset for HA may not be sufficient. More HA observations are required for adding HA/RN mixture type in the BHCA framework. The RN regions identified by the three methods generally agree well with each other.

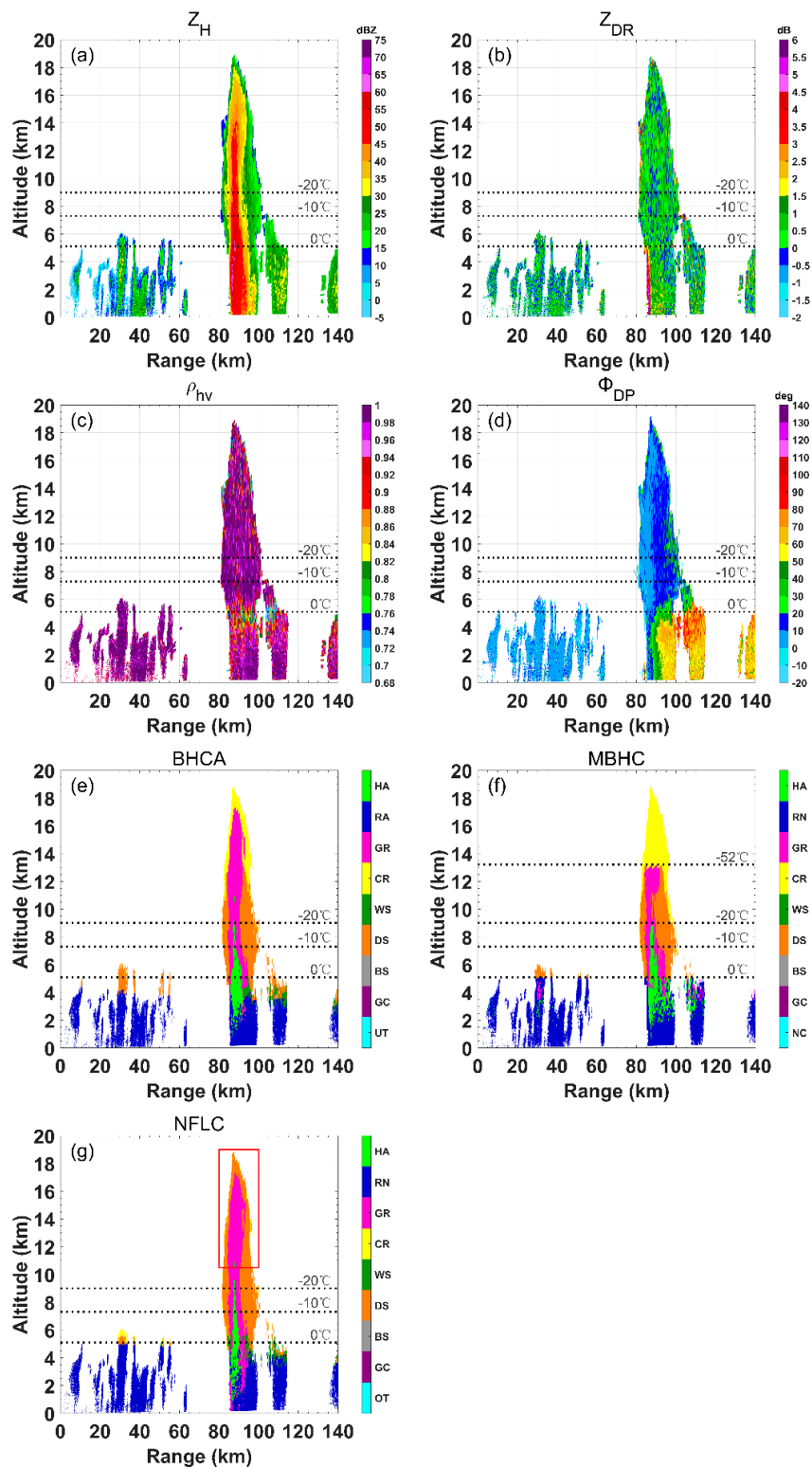


Figure 5. Range-height indicator (RHI) of (a) Z_H , (b) Z_{DR} , (c) ρ_{hv} , (d) Φ_{DP} , and corresponding hydrometeor classification results by the (e) Bayesian hydrometeor classification algorithm (BHCA), (f) Marzano-Bayesian hydrometeor classification algorithm (MBHC) and (g) NCAR fuzzy logic classifier (NFLC) at 128.6° azimuth, at 20:19 LST on 11 July 2014. The black dashed lines indicate the temperature level of 0 °C, -10 °C and -20 °C from bottom to top, respectively. The red rectangle highlights the differences in the classification results.

4.4. Biological Scatterers and Ground Clutter on 24 July 2014

At 08:03 (LST) on 24 July, 2014, a large area of BS and some GC were detected by NJU C-POL before the arrival of a typhoon outer rainband. A large area of high Z_{DR} (>4 dB) can be seen from Figure 6b with the color bar adjusted for large variation. The corresponding Z_H is between 5 and 30 dBZ; ρ_{hv} is less than 0.9 with some pixels even below 0.6; and SD (Φ_{DP}) is very high. These signatures suggest BS within this area. The BHCA identifies a large area of BS as expected and agrees well with that identified by the NFLC. There is a thin line extending from northwest to southwest, and further to south in Z_H , Z_{DR} , ρ_{hv} and Φ_{DP} (Figure 5a–d). These signatures are found to be caused by iron towers which are identified by both methods. There are a few pixels with high Z_H (Figure 6a), fluctuant Z_{DR} (Figure 6b), low ρ_{hv} (Figure 6c), high SD(Z_H) and SD(Φ_{DP}) (Figure 6d) near the radar site, suggesting these echoes are GC as well. These GC identified by the two methods are consistent with each other. The NFLC identifies some scattered GC in northwest and southeast of the radar site, which is identified as BS by the BHCA (red rectangle in Figure 6). These pixels show small SD(Z_H), which is more likely to be weather echoes or BS rather than GC [11], but the SD(Z_H) is not used by the NFLC. In addition, Z_{DR} shows high fluctuation in this area, which may largely contribute to the identification of GC by the NFLC.

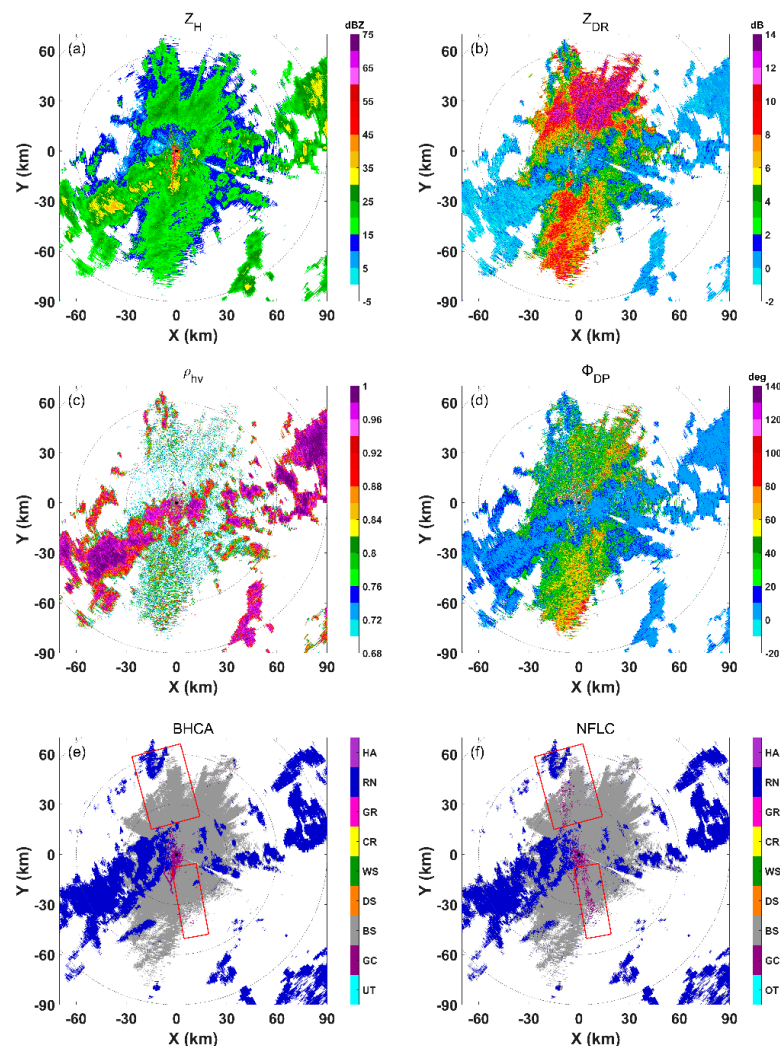


Figure 6. Plan position indicator (PPI) of (a) Z_H , (b) Z_{DR} , (c) ρ_{hv} , (d) Φ_{DP} , and corresponding hydrometeor classification results by (e) the Bayesian hydrometeor classification algorithm (BHCA) and (f) NCAR fuzzy logic classifier (NFLC) at 0.5° elevation angle at 08:03 LST on 24 July 2014 and hydrometeor classification results. The red rectangle highlights the different output classification.

4.5. Agreement Analysis

Table 5 shows the quantitative difference of each hydrometeor type identified by the BHCA, MBHC (Table 5a) and NFLC (Table 5b) during 20:04–22:57 LST on July 30 and 08:03–09:04 LST on 24 July, 2014, including both RHI and PPI data. A very small proportion of undefined type in the BHCA ($P(C_i|V_1, \dots, V_5)$ in Equation (2) $< 1.0 \times 10^{-30}$) is identified, which does not affect the comparison among the three classifiers, and thus not listed in Table 5. The values in Table 5a,b) represent the points (normalized by the total number of points along each row) classified as the hydrometeor types in the columns by the MBHC (NFLC) and the rows by the BHCA. Table 5a shows that there is good agreement between the MBHC and BHCA for RN (92%) and DS (92%). There is a good consistency (percentage $> 60\%$) between the NFLC and BHCA for RN (96%), GR (73%), WS (69%), DS (94%) and BS (93%), which is more consistent than that in Table 5a. The largest difference (13%) is found for the CR type in Table 5a, where 83% CR identified by the MBHC are classified as DS by the BHCA. This is because DS particles are not allowed to appear below -52°C due to the restriction of the prior PDF in MBHC, resulting in predominantly CR above that altitude in strong convection, and most of the CR below -52°C is classified as DS by the BHCA. A similar issue can be seen from Figure 5e–f. The agreement between the NFLC and BHCA for CR is also low (22%). This is due to the fact that the same membership function is used for CR and DS, resulting in much fewer CR samples produced by the NFLC. A large difference (31%) is also found for the HA type in Table 5a, while 33% HA identified by the MBHC is classified as RN by the BHCA, indicating a large difference in HA classification below the freezing level. This is partly due to the absence of RN/HA mixture type in the BHCA, while those echoes are identified as HA by the MBHC and RN by the BHCA. This is also the reason for the large difference of HA (Table 5b) identified by the BHCA and NFLC. In addition, the large prior PDF at high temperature also results in more HA identified by the MBHC within $10\text{--}20^\circ\text{C}$ than $3\text{--}10^\circ\text{C}$. A similar issue is found in GR type, which is the main reason why 20% GR (Table 5a) identified by the MBHC is classified as RN by the BHCA. The agreement in WS type is also low (34% in Table 5a) since most of BB is missed by the MBHC, resulting in very few WS dataset relative to that identified by the BHCA. Because the terrain around the radar site is flat, the GC dataset is rare. Most of the dataset of GC (Table 5b) is similar to Figure 5a–d. Therefore, echoes with low $SD(Z_H)$ and fluctuating Z_{DR} are also classified as GC by the NFLC, and the agreement of GC is moderate (51%) in Table 5b. Other than this, both the BHCA and NFLC do a reasonable job for GC classification.

Table 5. (a) Agreement of classification between the BHCA and MBHC during 18:04–22:57 LST on 30 July and 08:03–09:04 LST on 24 July, 2014. (The numbers in the table represent the percentages of the hydrometeor types in the column identified as the ones in the row. Bold font indicates good consistency); (b) Similar to Table 5a, but for agreement of classification between the BHCA and NFLC.

		BHCA								
Methods	Classes	HA	RN	GR	CR	WS	DS	BS	GC	
a	MBHC	HA	31%	33%	21%	0%	2%	11%	-	-
		RN	0%	92%	0%	0%	3%	3%	-	-
		GR	2%	20%	51%	0%	16%	11%	-	-
		CR	0%	0%	4%	13%	0%	83%	-	-
		WS	2%	2%	14%	0%	34%	48%	-	-
		DS	0%	0%	6%	1%	0%	92%	-	-
b	NFLC	HA	57%	37%	6%	0%	0%	0%	0%	0%
		RN	0%	96%	1%	0%	1%	2%	0%	0%
		GR	6%	12%	73%	0%	1%	2%	0%	0%
		CR	0%	2%	0%	22%	0%	76%	0%	0%
		WS	0%	16%	9%	0%	69%	6%	0%	0%
		DS	0%	0%	4%	2%	1%	94%	0%	0%
		BS	0%	4%	0%	0%	0%	0%	93%	3%
GC	0%	5%	0%	0%	0%	1%	43%	51%		

5. Conclusions

A new hydrometeor classification algorithm is developed based on Bayes' theorem. The CLPDFs of radar variables and prior PDFs of each hydrometeor types are constructed with training data, which are manually selected by experts and the classification results from RCHIA [12]. The prior PDFs in this method include not only temperature information but also background information about the occurrence frequency of different hydrometeor types at each altitude.

The performance of this BHCA approach is compared with the MBHC [24] and the widely used NFLC [16] using NJU C-POL observations from the OPACC field campaign in 2014. The testing data include a squall line with trailing stratiform precipitation, isolated strong convection, and GC and BS observations from both PPI and RHI scans. The results show that the BHCA produces a more reasonable classification output than the MBHC and NFLC over the Yangtze-Huaihe River Basin, Eastern China. CR within strong isolated convection are largely missed by the NFLC, which may be related to an inappropriate membership function. WS are almost missed by the MBHC due to large uncertainty in modelling the melting hydrometeor. The prior PDFs in the MBHC have two limitations when the algorithm is applied to the strong convection over YHRB, Eastern China. One is that the prior PDFs for GR and DS below $-52\text{ }^{\circ}\text{C}$ seem not realistic in this study. The other is that the prior PDFs for HA and GR are larger within $10\text{--}20\text{ }^{\circ}\text{C}$ than $3\text{--}10\text{ }^{\circ}\text{C}$, which may result in unexpected HA and GR within area of $10\text{--}20\text{ }^{\circ}\text{C}$ even though it is a favorable temperature range for melting rather than riming and deposition. The BHCA overcomes the two shortcomings in the prior PDFs and produces an overall reasonable classification.

To avoid the circular reasoning in this paper, the radar data used for training and testing are separated out. The training and testing datasets are also processed by different methods. Nevertheless, subjective information still exists in the training dataset and validation procedure. We hope to have the chance to do an objective validation with in-situ observations in the future. In addition, future work will include more observations to build a robust CLPDF for HA and possibly additional hydrometeor types in the BHCA.

Author Contributions: Conceptualization, project administration and supervision, K.Z. and G.Z.; methodology and writing—original draft preparation, J.Y.; data curation, G.C. and H.H.; writing—review and editing, H.C.

Funding: This work was primarily supported by the National Key Research and Development Program of China (Grant Nos. 2017YFC1501703 and 2018YFC1506404), the National Natural Science Foundation of China (grants 41875053, 41805025, 41475015, 41322032 and 41805015), the Open Research Program of the State Key Laboratory of Severe Weather, and the Key Research Development Program of Jiangsu Science and Technology Department (Social Development Program, No. BE2016732), and the National 973 Project (2013CB430101).

Acknowledgments: Observational data used in this study were collected by a National 973 Project (2013CB430101), and the requests for the data can be made at <http://scw973.nju.edu.cn/> or by contacting the project office via yang.zhengwei@nju.edu.cn.

Conflicts of Interest: The authors declare no conflict of interest.

References

1. Straka, J.M.; Zrnić, D.S.; Ryzhkov, A.V. Bulk hydrometeor classification and quantification using polarimetric radar data: synthesis of relations. *J. Appl. Meteorol.* **2000**, *39*, 1341–1372. [[CrossRef](#)]
2. Ryzhkov, A.V.; Zrnić, D.S. Discrimination between rain and snow with a polarimetric radar. *J. Appl. Meteorol.* **1998**, *37*, 1228–1240. [[CrossRef](#)]
3. Zrnić, D.A.S.; Ryzhkov, A.; Straka, J.; Liu, Y.; Vivekanandan, J. Testing a procedure for automatic classification of hydrometeor types. *J. Atmos. Ocean. Technol.* **2001**, *18*, 892–913. [[CrossRef](#)]
4. Kumjian, M.R.; Deierling, W. Analysis of thundersnow storms over Northern Colorado. *Weather Forecast.* **2015**, *30*, 1469–1490. [[CrossRef](#)]
5. Wen, J.; Zhao, K.; Huang, H.; Zhou, B.; Yang, Z.; Chen, G.; Wang, M.; Wen, L.; Dai, H.; Xu, L.; et al. Evolution of microphysical structure of a subtropical squall line observed by a polarimetric radar and a disdrometer during OPACC in Eastern China. *J. Geophys. Res. Atmos.* **2017**, *122*, 8033–8050. [[CrossRef](#)]

6. Ryzhkov, A.V.; Kumjian, M.R.; Ganson, S.M.; Zhang, P. Polarimetric Radar Characteristics of Melting Hail. Part II: Practical Implications. *J. Appl. Meteorol. Climatol.* **2013**, *52*, 2871–2886. [[CrossRef](#)]
7. Wang, J.; Zhou, S.; Yang, B.; Meng, X.; Zhou, B. Nowcasting cloud-to-ground lightning over Nanjing area using S-band dual-polarization doppler radar. *Atmos. Res.* **2016**, *178*, 55–64. [[CrossRef](#)]
8. Mahale, V.N.; Zhang, G.; Xue, M. Fuzzy Logic Classification of S-band polarimetric radar echoes to identify three-body scattering and improve data quality. *J. Appl. Meteorol. Climatol.* **2014**, *53*, 2017–2033. [[CrossRef](#)]
9. Giangrande, S.E.; Ryzhkov, A.V. Estimation of rainfall based on the results of polarimetric echo classification. *J. Appl. Meteorol. Climatol.* **2008**, *47*, 2445–2462. [[CrossRef](#)]
10. Dolan, B.; Rutledge, S.A. A Theory-based hydrometeor identification algorithm for X-band polarimetric radars. *J. Atmos. Ocean. Technol.* **2009**, *26*, 2071–2088. [[CrossRef](#)]
11. Park, H.S.; Ryzhkov, A.V.; Zrnić, D.S.; Kim, K.-E. The hydrometeor classification algorithm for the polarimetric WSR-88D: Description and application to an MCS. *Weather Forecast.* **2009**, *24*, 730–748. [[CrossRef](#)]
12. Dolan, B.; Rutledge, S.A.; Lim, S.; Chandrasekar, V.; Thurai, M. A Robust C-band hydrometeor identification algorithm and application to a long-term polarimetric radar dataset. *J. Appl. Meteorol. Climatol.* **2013**, *52*, 2162–2186. [[CrossRef](#)]
13. Liu, H.; Chandrasekar, V. Classification of hydrometeors based on polarimetric radar measurements: development of fuzzy logic and neuro-fuzzy systems, and in situ verification. *J. Atmos. Ocean. Technol.* **2000**, *17*, 140–164. [[CrossRef](#)]
14. Marzano, F.S.; Scaranari, D.; Vulpiani, G. Supervised fuzzy-logic classification of hydrometeors using C-band weather radars. *IEEE Trans. Geosci. Remote Sens.* **2007**, *45*, 3784–3799. [[CrossRef](#)]
15. Snyder, J.C.; Ryzhkov, A.V. Automated detection of polarimetric tornadic debris signatures using a hydrometeor classification algorithm. *J. Appl. Meteorol. Climatol.* **2015**, *54*, 1861–1870. [[CrossRef](#)]
16. Vivekanandan, J.; Zrnić, D.S.; Ellis, S.M.; Oye, R.; Ryzhkov, A.V.; Straka, J. Cloud microphysics retrieval using S-band dual-polarization radar measurements. *Bull. Am. Meteorol. Soc.* **1999**, *80*, 381–388. [[CrossRef](#)]
17. Lim, S.; Chandrasekar, V.; Bringi, V.N. Hydrometeor classification system using dual-polarization radar measurements: Model improvements and in situ verification. *IEEE Trans. Geosci. Remote Sens.* **2005**, *43*, 792–801. [[CrossRef](#)]
18. Wen, G.; Protat, A.; May, P.T.; Wang, X.; Moran, W. A cluster-based method for hydrometeor classification using polarimetric variables. Part I: interpretation and analysis. *J. Atmos. Ocean. Technol.* **2015**, *32*, 1320–1340. [[CrossRef](#)]
19. Kouketsu, T.; Uyeda, H.; Ohigashi, T.; Oue, M.; Takeuchi, H.; Shinoda, T.; Tsuboki, K.; Kubo, M.; Muramoto, K.-I. A hydrometeor classification method for X-band polarimetric radar: Construction and validation focusing on solid hydrometeors under moist environments. *J. Atmos. Ocean. Technol.* **2015**, *32*, 2052–2074. [[CrossRef](#)]
20. Wen, G.; Protat, A.; May, P.T.; Moran, W.; Dixon, M. A cluster-based method for hydrometeor classification using polarimetric variables. Part II: Classification. *J. Atmos. Ocean. Technol.* **2016**, *33*, 45–60. [[CrossRef](#)]
21. Al-Sakka, H.; Boumahmoud, A.-A.; Fradon, B.; Frasier, S.J.; Tabary, P. A New fuzzy logic hydrometeor classification scheme applied to the french X-, C-, and S-band polarimetric radars. *J. Appl. Meteorol. Climatol.* **2013**, *52*, 2328–2344. [[CrossRef](#)]
22. Bechini, R.; Chandrasekar, V. A Semisupervised robust hydrometeor classification method for dual-polarization radar applications. *J. Atmos. Ocean. Technol.* **2014**, *32*, 22–47. [[CrossRef](#)]
23. Marzano, F.S.; Scaranari, D.; Montopoli, M.; Vulpiani, G.; Anagnostou, M.N.; Anagnostou, E.N. Bayesian classification of hydrometeors from polarimetric radars at S- and X- bands: algorithm design and experimental comparisons. In Proceedings of the 2007 IEEE International Geoscience and Remote Sensing Symposium, Barcelona, Spain, 23–28 July 2007; pp. 4156–4159.
24. Marzano, F.S.; Scaranari, D.; Montopoli, M.; Vulpiani, G. Supervised classification and estimation of hydrometeors from C-band dual-polarized radars: A Bayesian approach. *IEEE Trans. Geosci. Remote Sens.* **2008**, *46*, 85–98. [[CrossRef](#)]
25. Gourley, J.J.; Tabary, P.; Parent du Chatelet, J. A fuzzy logic algorithm for the separation of precipitating from nonprecipitating echoes using polarimetric radar observations. *J. Atmos. Ocean. Technol.* **2007**, *24*, 1439–1451. [[CrossRef](#)]
26. Bukovčić, P.; Zrnić, D.; Zhang, G. Convective–stratiform separation using video disdrometer observations in central Oklahoma—The Bayesian approach. *Atmos. Res.* **2015**, *155*, 176–191. [[CrossRef](#)]

27. Xue, M. Preface to the special issue on the “Observation, prediction and analysis of severe convection of China” (OPACC) national “973” Projec. *Adv. Atmos. Sci.* **2016**, *33*, 1099–1101. [[CrossRef](#)]
28. Huang, H.; Zhang, G.; Zhao, K.; Giangrande, S. A Hybrid method to estimate specific differential phase and rainfall with linear programming and physics constraints. *IEEE Trans. Geosci. Remote Sens.* **2016**, *55*, 1–16. [[CrossRef](#)]
29. Sampe, T.; Xie, S.-P. Large-scale dynamics of the Meiyu-Baiu rainband: Environmental forcing by the westerly jet. *J. Clim.* **2010**, *23*, 113–134. [[CrossRef](#)]
30. Wang, Y.; Chandrasekar, V. Algorithm for estimation of the specific differential phase. *J. Atmos. Ocean. Technol.* **2009**, *26*, 2565–2578. [[CrossRef](#)]
31. Bringi, V.N.; Chandrasekar, V.; Balakrishnan, N.; Zrnic, D.S. An examination of propagation effects in rainfall on radar measurements at microwave frequencies. *J. Atmos. Ocean. Technol.* **1990**, *7*, 829–840. [[CrossRef](#)]
32. Berenguer, M.; Sempere-Torres, D.; Corral, C.; Sánchez-Diezma, R. A fuzzy logic technique for identifying nonprecipitating echoes in radar scans. *J. Atmos. Ocean. Technol.* **2006**, *23*, 1157–1180. [[CrossRef](#)]
33. Cho, Y.-H.; Lee, G.W.; Kim, K.-E.; Zawadzki, I. Identification and removal of ground echoes and anomalous propagation using the characteristics of radar echoes. *J. Atmos. Ocean. Technol.* **2006**, *23*, 1206–1222. [[CrossRef](#)]
34. Hubbert, J.C.; Dixon, M.; Ellis, S.M. Weather radar ground clutter. Part II: Real-time identification and filtering. *J. Atmos. Ocean. Technol.* **2009**, *26*, 1181–1197. [[CrossRef](#)]
35. Elmore, K.L. The NSSL hydrometeor classification algorithm in winter surface precipitation: Evaluation and future development. *Weather Forecast.* **2011**, *26*, 756–765. [[CrossRef](#)]
36. Thompson, E.J.; Rutledge, S.A.; Dolan, B.; Chandrasekar, V.; Cheong, B.L. A dual-polarization radar hydrometeor classification algorithm for winter precipitation. *J. Atmos. Ocean. Technol.* **2014**, *31*, 1457–1481. [[CrossRef](#)]
37. Schuur, T.J.; Park, H.-S.; Ryzhkov, A.V.; Reeves, H.D. Classification of precipitation types during transitional winter weather using the RUC model and polarimetric radar retrievals. *J. Appl. Meteorol. Climatol.* **2012**, *51*, 763–779. [[CrossRef](#)]
38. Snyder, J.C.; Bluestein, H.B.; Zhang, G.; Frasier, S.J. Attenuation correction and hydrometeor classification of high-resolution, X-band, dual-polarized mobile radar measurements in severe convective storms. *J. Atmos. Ocean. Technol.* **2010**, *27*, 1979–2001. [[CrossRef](#)]
39. Meneghini, R.; Liang, L. Dielectric constants for melting hydrometeors as derived from a numerical method. In Proceedings of the IGARSS '96. 1996 International Geoscience and Remote Sensing Symposium, Lincoln, NE, USA, 31 May 1996; pp. 16–18.
40. Carey, L.D.; Rutledge, S.A. The relationship between precipitation and lightning in tropical island convection: A C-band polarimetric radar study. *Mon. Weather Rev.* **2000**, *128*, 2687–2710. [[CrossRef](#)]
41. Rowe, A.K.; Houze, R.A., Jr. Microphysical characteristics of MJO convection over the Indian Ocean during DYNAMO. *J. Geophys. Res. Atmos.* **2014**, *119*, 2543–2554. [[CrossRef](#)]

